Contents lists available at ScienceDirect

Microchemical Journal

journal homepage: www.elsevier.com/locate/microc

The ultrasensitive detection of *p*-nitrophenol using a simple activated carbon electrode modified with electrodeposited bismuth dendrites

Tian Yu [a], Karen Herdman [a], Palanisamy Rupa Kasturi [a], Carmel B. Breslin [a,b,*]

[a] *Department of Chemistry, Maynooth University, Maynooth, Co. Kildare, Ireland*
[b] *Kathleen Lonsdale Institute, Maynooth University, Maynooth, Co. Kildare, Ireland*

A B S T R A C T

Bismuth dendrites were electrodeposited onto an activated glassy carbon electrode and the resulting modified electrode was employed in the electrochemical detection of *para*-nitrophenol, an aromatic aquatic pollutant. The carbon electrode was activated by cycling between -2.0 and 2.0 V vs. SCE to create active sites that can promote the electron transfer reaction. Bismuth dendrites were subsequently deposited at a potential of -1.0 V vs. SCE for 400 s. A near 5-fold increase in the peak current associated with the conversion of *para*-nitrophenol (100 μM) to *para*-hydroxyaminophenol was obtained on activating the glassy carbon electrode. A more impressive 7-fold increase in the peak current was achieved on decorating the activated glassy carbon with bismuth dendrites. Calibration curves with linear regions from 1.6 to 170 μM and between 0.005 and 1.6 μM *para*-nitrophenol were obtained to give a LOD value of 0.18 nM and a sensitivity of 29.4 μA μM^{-1} cm^{-2} for the lower concentration range. Good repeatability, reproducibility and selectivity were achieved, while recovery values between 96.5 and 106.7 % were obtained in water samples. In addition, the bismuth dendrites were easily regenerated through an oxidation step at 0.6 V vs. SCE followed by a 400 s electrodeposition period in 1.0 mM Bi(III).

1. Introduction

Nitrophenols, and especially *para*-nitrophenol (*p*-NP) or 4-nitrophenol, have long been known and recognised as priority pollutants in aquatic environments [1]. They are employed as precursors in the formation of dyes and indicators, pesticides, pharmaceuticals, and explosives and have the potential to enter the environment through the discharge of industrial wastewater [2]. Indeed, concentrations in the vicinity of 0.43 μg L^{-1} have been reported in rivers in Europe [3]. The *p*-NP isomer has a high solubility in water, it is severely toxic and is a threat to all aquatic life and ecological environments. In particular, the nitro group is readily reduced by enzymes to produce a nitro radical anion, which in turn can generate a hydroxylamine derivative, which exerts mutagenic and carcinogenic effects [4,5]. Accordingly, the concentration levels of *p*-NP in aquatic environments are especially important. For example the lethal (LC$_{50}$) concentration, which is a good indicator of the acute toxicity of a pollutant, reflecting its concentration that kills 50 % of species, has been obtained for a number of aquatic species exposed to *p*-NP. The LC$_{50}$ value has been reported as 540 μg L^{-1} for *D. carinata* (equivalent to 3.88 μM) over a 24 h exposure period to *p*-NP [6], while the LC$_{50}$ values are 56 μg L^{-1} (0.40 μM) for Daphnia and

92 μg L^{-1} (0.66 μM) for Carp [7]. Likewise, Yan et al. [8] determined the acute and chronic concentrations of algae exposed to *p*-NP as 2180 and 218.0 μg L^{-1}, respectively. Therefore, the detection of *p*-NP at concentrations in the vicinity of nM to low μM is particularly relevant in monitoring the quality of aquatic systems.

Several analytical techniques such as high performance liquid chromatography (HPLC) [9,10], gas chromatography [11] and spectrophotometry [12] can be employed in the detection of *p*-NP. Nevertheless, they are not always suitable for the rapid and on-site analysis of water samples. On the other hand, sensors and especially electrochemical sensors are attractive as they are simple to operate and are ideal for on-site analytical measurements. Indeed electrochemical sensors have been investigated extensively with several reports in the literature describing the electrochemical detection of *p*-NP [13–16]. These sensors are typically produced using metal oxide nanostructures [15], MXenes [13] or two dimensional layered materials [14] that can be time-consuming to fabricate. Moreover, they do not always provide a sufficiently low detection in the nM region for *p*-NP. For example, a CeFeP modified glassy carbon electrode (GCE) showed a linear range to 0.1 μM [16], while detection limits of 0.61 and 2.88 μM were observed with CuBi$_2$O$_4$ [15] and reduced graphene oxide coupled with tungsten
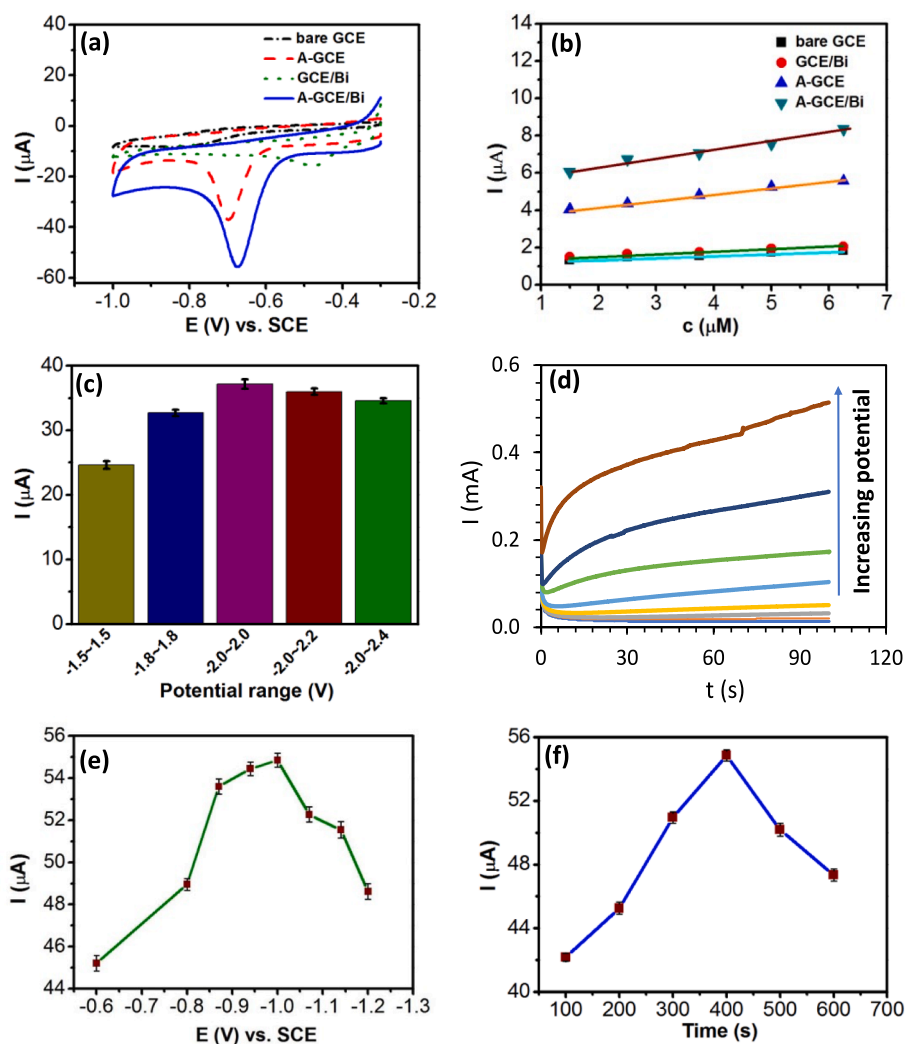

Fig. 1. **(a)** CVs recorded for GCE, A-GCE, GCE/Bi and A-GCE/Bi in 100 μM *p*-NP; **(b)** peak currents plotted against the *p*-NP concentration; **(c)** peak current recorded in 100 μM *p*-NP as a function of the activation potential ranges used to form A-GCE; **(d)** current–time transients recorded at –0.75 V, –0.80 V, –0.85 V, –0.90 V, –0.95 V, –1.0 V, –1.05 V and –1.10 V recorded in 1.0 mM $Bi(NO_3)_3$ at a pH of 1.5; **(e)** peak current recorded in 100 μM *p*-NP as a function of the electrodeposition potential and **(f)** electrodeposition time at −1.0 V during the deposition of bismuth.

oxide [14], respectively.

Recently, it has been shown that when GCE electrodes are activated/ oxidised by cycling to potentials beyond the oxygen evolution reaction, they become very effective in facilitating electron transfer, making them attractive in the design of electrochemical-based sensors [17–20]. This has been attributed to the generation of oxygen-based functional groups, which are formed as the C–C bonds are attacked by •OH radicals, which are generated at the high potentials [21]. Another interesting approach is the utilisation of bismuth, which is non-toxic. Indeed, electro-deposited bismuth films and nanostructures have been used in the electroanalysis of metronidazole [22] and various heavy metal ions [23–25]. It has been shown that bismuth modified electrodes exhibit high overpotentials for the hydrogen evolution reaction and have low background currents. This makes bismuth interesting in the electro-chemical reduction of analytes, where the adsorption and reduction of hydrogen ions may be a competing reaction.

In this paper we show that a glassy carbon electrode (GCE) can be easily activated using an electrochemical cycling process and then modified with bismuth dendrites using a simple electrodeposition routine. No drop-casting of electrocatalysts is required, where it can be difficult to achieve reproducible and uniform surfaces. Moreover, the sensor can be easily regenerated by oxidising and removing the bismuth

dendrites followed by their subsequent electrodeposition. Finally, this sensor is very well suited to monitoring *p*-NP in water and in different aquatic environments at low μM and nM concentrations.

2. Experimental

Analytical grade chemicals, obtained from Merck/Sigma Aldrich, were used as received and consisted of phosphate salts to prepare buffers, bismuth nitrate, *p*-NP, sulfate, carbonate and acetate salts. The electrochemical experiments were performed using a Solartron 1287 potentiostat, a Solartron 1287 potentiostat coupled with a 1255 FRA and a CHI potentiostat, for cyclic voltammetry (CV), electrochemical impedance and differential pulse voltammetry (DPV) experiments, respectively. The surface morphology experiments were performed using SEM (scanning electron microscopy) and EDX (energy dispersive X-ray analysis) with a Hitachi S–3200–N microscope and an Oxford Instrument INCAz-act ESX. The SEM micrographs were recorded using the modified glassy carbon electrodes (activated with the electro-deposited bismuth dendrites). The electrodes were held in place in the vacuum chamber using a custom-made electrode holder and imaged directly.

A three-electrode electrochemical cell was used in all experiments. A

3 mm GCE (with a geometric surface area of 0.0707 cm^2), a saturated calomel reference electrode (SCE) and a high surface area platinum wire were employed as the electrodes. The GCE was polished using a 1 μm particle sized diamond suspension (Akasol), then sonicated, rinsed thoroughly with deionised water and dried. Four electrodes were prepared, the bare unmodified GCE, the bismuth modified GCE (GCE/Bi), the activated GCE (A-GCE) and the bismuth modified A-GCE (A-GCE/Bi). The GCE/Bi was prepared by immersing the cleaned GCE in a 1.0 mM Bi(NO$_3$)$_3$ solution dissolved in HNO$_3$ and adjusted to a pH of 1.5 by mixing with CH$_3$COONa and CH$_3$COOH (pH 4.4) and applying a potential of −1.0 V vs. SCE for 400 s to reduce the Bi(III). The activated GCE (A-GCE) was formed in a 0.1 M phosphate buffer (pH = 6.0) by cycling at 100 mV s^{-1} between –2.0 V and 2.0 V vs. SCE for 30 cycles. After activation, the A-GCE was washed with deionised water and dried. The A-GCE//Bi was formed through the electrodeposition of bismuth onto the A-GCE in the acidified 1.0 mM Bi(NO$_3$)$_3$ at −1.0 V vs. SCE for 400 s.

Unless otherwise stated, the CV data were recorded at 50 mV s^{-1}, and the DPV data were recorded with a pulse amplitude of 50 mV, a pulse width of 0.05 s, sampling width of 0.0167 s, and a pulse period of 0.50 s. The impedance data were collected at applied potentials where the reduction of *p*-NP occurred, i.e., at −0.8 V vs. SCE for bare GCE, −0.5 V vs. SCE for GCE/Bi, −0.7 V vs. SCE for A-GCE and −0.68 V vs. SCE for A-GCE/Bi in the buffered 100 μM *p*-NP solution, using a perturbation potential of 10 mV. The data were recorded after a 30 min period at the required potential. All solutions were deoxygenated with high purity nitrogen gas for a 30 min period prior to the electrochemical measurements. All experiments were performed in triplicate and using the standard deviation (σ) and number of experiments performed (n) the standard error was computed as $\sigma/n^{1/2}$.

3. Results and discussion

3.1. Selection of modified electrodes

A comparison of the four electrodes in the electrochemical reduction of *p*-NP to p-hydroxyaminophenol is illustrated in Fig. 1. It is clearly evident in Fig. 1(a) that the A-GCE/Bi gives the highest peak current and performs best in the detection of *p*-NP. The bare GCE exhibits a broad reduction wave at about –0.80 V vs. SCE, with a low peak current of 7.82 μA. On activating the GCE (A-GCE), a sharper peak with a higher peak current (36.82 μA) is achieved and the peak potential is shifted to a more thermodynamically favourable value of ca. –0.70 V vs. SCE. An even greater shift in the peak potential is seen when bismuth is electrodeposited onto the surface, with a peak potential of −0.50 V vs. SCE, but with a somewhat low peak current. However, when bismuth is electrodeposited onto the activated GCE to give A-GCE/Bi, a much higher peak current of 55.62 μA is obtained. Although the peak potential is considerably lower than the GCE/Bi, the reduction peak potential of –0.68 V vs. SCE compares very well to some recently reported materials that have been employed to detect *p*-NP with peak potentials varying from –0.73 V vs. Ag/AgCl [26] to –0.77 V vs. Ag/AgCl [27]. The ability of these four electrodes to detect *p*-NP is more clearly evident in Fig. 1(b) where the peak current is shown at lower *p*-NP concentrations from 1.5 to 6.5 μM. Here, the A-GCE/Bi provides the highest gradient of 0.48 μA μM^{-1}, while lower values of 0.32 μA μM^{-1} for A-GCE and 0.12 μA μM^{-1} for GCE/Bi were seen, highlighting the advantage of combining the electrodeposition of bismuth with the activated GCE.

The influence of the activation process is summarised in Fig. 1(c) where it is evident that optimum activation occurs by cycling the GCE between the potentials of –2.0 V and 2.0 V vs. SCE at 100 mV s^{-1} for 30 cycles. With higher upper potentials of 2.2 and 2.4 V vs. SCE, somewhat lower peak currents are seen and this is coupled with more capacitive background currents. The current–time transients recorded during the electrodeposition of bismuth are shown in Fig. 1(d). It is clear that the rate of electrodeposition increases on applying more negative potentials.

Table 1
Reproducibility of GCE/Bi, A-GCE and A-GCE/Bi in the detection of *p*-NP.

100 μM *p*-NP	Peak Current (μA)					RSD (%) (n = 5)
	1	2	3	4	5	
GCE/Bi	15.9	14.9	15.5	14.6	15.2	3.33
A-GCE	37.8	35.9	36.7	37.5	36.8	2.01
A-GCE/Bi	56.3	55.8	54.9	54.1	55.5	1.53

On application of the potential there is a sharp increase in the current, which then decays due to the charging of the double layer. This is then followed by nucleation and growth of the bismuth deposits. Interestingly, there is no evidence for the overlapping of nuclei, as the nucleation current continues to increase with increasing deposition periods. At the higher overpotentials there is evidence of the competing hydrogen ion reduction reaction, and this is clearly seen at –1.1 V vs. SCE.

It was found that the optimum bismuth electrodeposition period at the activated GCE was 400 s at a fixed potential of –1.0 V. This is illustrated in Fig. 1(f), where the highest peak currents can be obtained with a 400 s electrodeposition period. This optimum deposition time gives rise to a 51 % increase in the peak current for A-GCE/Bi compared to A-GCE. In addition, the influence of the electrodeposition potential is summarised in Fig. 1(e), where electrodeposition at –1.0 V gives the highest peak current. The sharp decrease in the *p*-NP reduction peak current, which is evident at –1.2 V vs. SCE, is probably related to the competing hydrogen ion reduction reaction in the acidic Bi(III) solution. This competing reaction will lead to lower amounts of electrodeposited bismuth and may also alter the nature of the bismuth deposits. The electrodeposition of Bi(III) was studied further by altering the pH of the solution, and the optimum pH was found to be at a value of 1.5. Indeed, higher pH values gave rise to the precipitation of bismuth hydroxides.

The reproducibility of the A-GCE, GCE/Bi and A-GCE/Bi as sensors is summarised in Table 1. These data were recorded in a neutral and buffered 100 μM *p*-NP solution. Very good reproducibility is evident with all three sensors, with RSD values varying between 1.53 and 3.33 %. It is also evident from this table that the A-GCE/Bi has the lowest error, with the RSD at the relatively low value of 1.53 %.

3.2. Characterisation studies

The surface morphology of the A-GCE/Bi, GCE and A-GCE is shown in Fig. 2. The images in Fig. 2(a) and (b), which represent the A-GCE/Bi electrode, indicate the formation of bismuth dendrites that are dispersed across the surface. These images are very different to the activated GCE, Fig. 2(c). The A-GCE shows evidence of surface dissolution, resembling pitting attack and these pits are uniformly dispersed across the surface. This is consistent with previous studies where it has been reported that carbon-based substrates can be oxidised when polarised at high potentials beyond the oxygen evolution reaction [17–20]. At these high potentials, OH$^{\bullet}$ radicals are formed and these can attack the C–C bonds to give oxygen-containing groups [21]. Indeed, it has been suggested that these oxygenated species facilitate and increase the rate of electron transfer and this is consistent with the data presented in Fig. 1(a). In Fig. 2(d), the bare GCE is evident and is free from any surface attack. The EDX spectrum presented in the inset of Fig. 2(d) shows the spectrum of the A-GCE/Bi, with clear indications for the presence of Bi. The oxygen occurs mainly from the oxygenated species that are present on the A-GCE. Mapping experiments are shown in Fig. 2 for carbon (C), bismuth (Bi), and oxygen (O) and it is clear that the bismuth and oxygen are reasonably well distributed over the surface.

The impedance spectra of the different electrodes recorded in the presence of 100 μM *p*-NP is shown in Supplementary Information, Fig. S1. These data were recorded at a fixed potential that coincides with the peak potentials observed in the voltammograms for the reduction of *p*-NP. In this analysis, the experimental data are depicted as symbols,
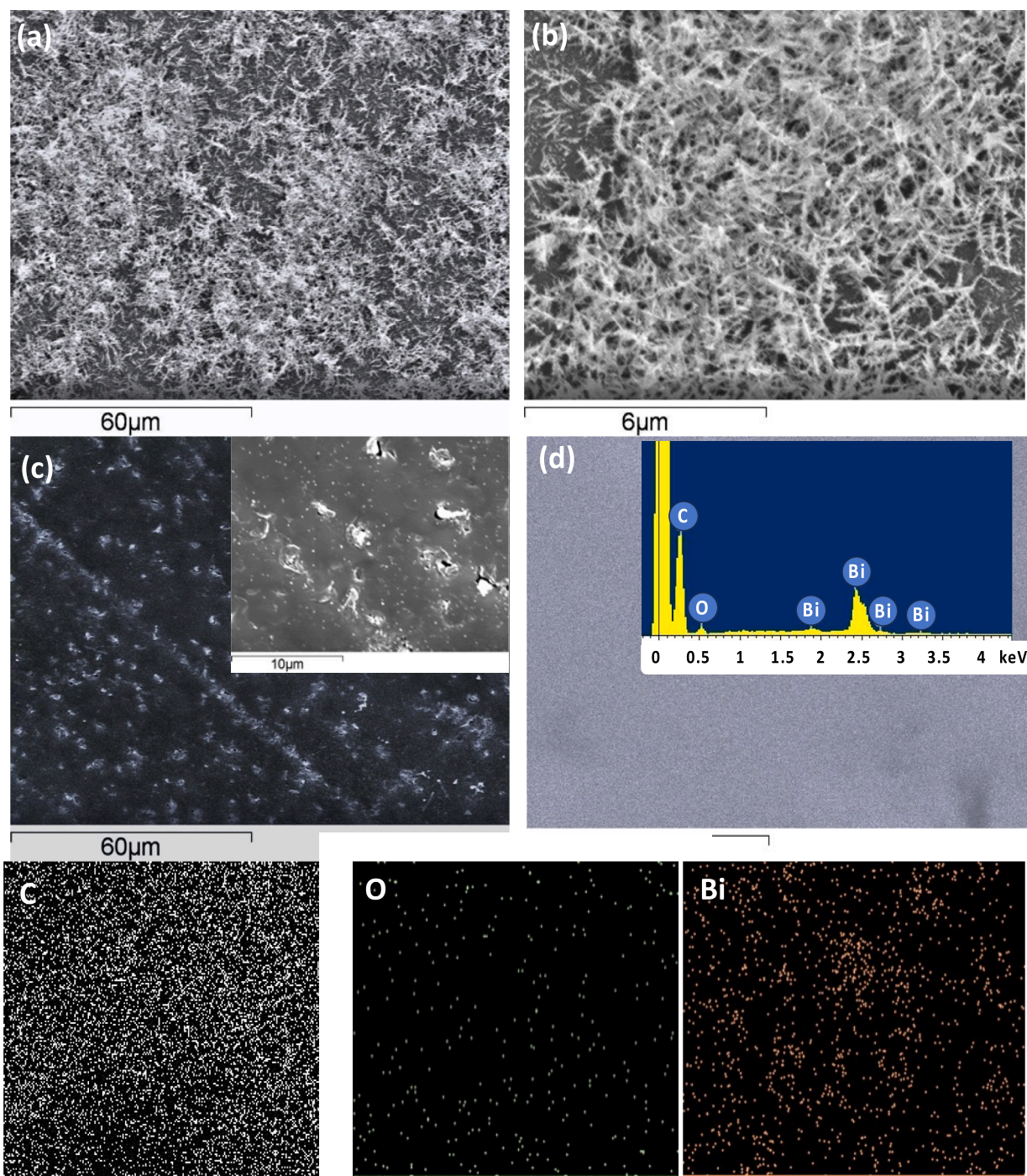
Fig. 2. SEM micrographs recorded for A-GCE/Bi at **(a)** low and **(b)** higher magnification; **(c)** micrographs recorded for A-GCE; **(d)** micrographs for unmodified GCE with EDX spectrum recorded for A-GCE/Bi in the inset, and mapping data for C, O and Bi.

while the fitted data are shown as continuous traces. All data were fitted using the equivalent circuit provided in Fig. S1. Here, the solution resistance is represented as R_1, the charge-transfer resistance is denoted as R_2, while the CPE elements represent constant phase elements, with CPE1 corresponding to the double layer capacitance and CPE2 indicating diffusional processes. The impedance profiles are similar showing a semicircle at higher frequencies and a diffusion tail at lower frequencies, with little indications that the electrodeposition of the bismuth dendrites give rise to any reduction in the charge transfer resistance. Indeed, the lowest charge-transfer resistance of 6073 ± 342

Ω was obtained for the A-GCE. On the electrodeposition of the bismuth dendrites an increase in the charge transfer resistance was observed, with a 12 % increase seen on the electrodeposition of bismuth at the A-GCE and a 10 % increase evident on modifying the bare GCE with the bismuth dendrites. The highest capacitance (CPE1 with n > 0.86) was observed with the activated electrodes, with a value of 23.11 ± 0.45 µF for the A-GCE/Bi and 26.58 ± 0.72 µF for the A-GCE and this is consistent with the generation of oxygenated groups during the activation process.
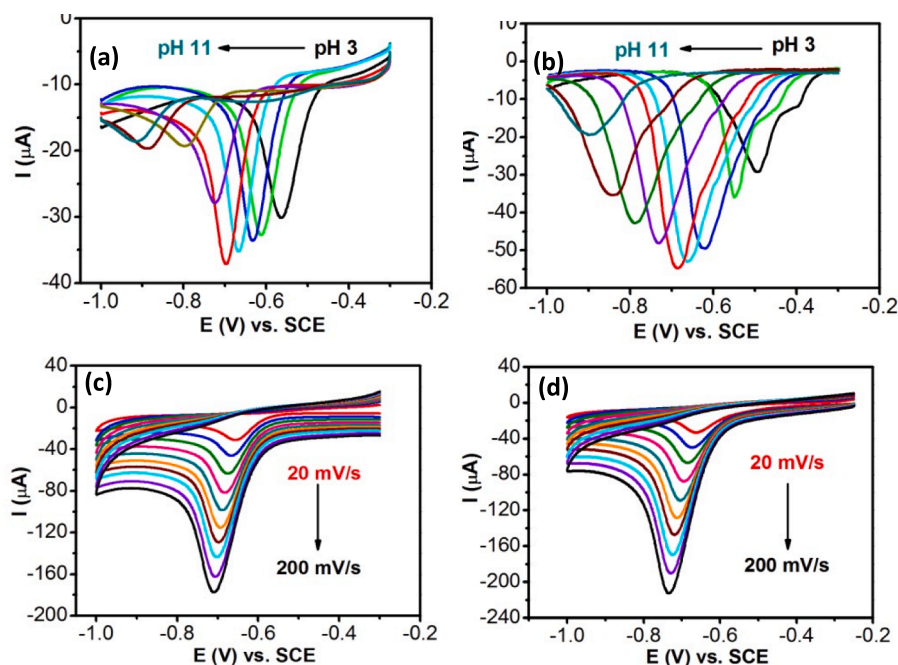
Fig. 3. DPVs recorded in 100 μM *p*-NP as a function of pH for **(a)** A-GCE and **(b)** A-GCE/Bi and **(c)** CVs recorded at scan rates from 20 to 200 mV s^{-1} for A-GCE and **(d)** A-GCE/Bi.

3.3. Influence of pH, adsorption-like behaviour and kinetics

The influence of the pH of the electrolyte on the reduction of *p*-NP was studied at both the A-GCE and A-GCE/Bi. It was found that the pH had a significant influence on the reduction peak potential as shown in Fig. 3(a) for A-GCE and in Fig. 3(b) for A-GCE/Bi, with the peak potential shifting to lower potentials on increasing the pH of the solution. On plotting the peak potential as a function of the pH (Fig. S2(a) and (b)) linear plots were obtained, and the linear regression equations were deduced as $E_p = -0.047$ pH $- 0.39$ ($R^2 = 0.98$) for the A-GCE and $E_p = -0.049$ pH -0.35 ($R^2 = 0.99$) for the A-GCE/Bi. These slopes are in reasonable agreement with the Nernst equation, where at 298 K, the theoretical slope is predicted as -0.0591 V/pH for the transfer of equal numbers of protons and electrons. This is consistent with the transfer of four electrons and four protons with the conversion of the $-NO_2$ group to $-NHOH$. The optimum pH for both electrodes was about a pH of 7.0, while lower peak currents were evident at more acidic and alkaline pH values, Fig. S2(c) and (d).

Scan rate studies were carried out to determine if the electrochemical reduction of *p*-NP was under diffusion or adsorption control. The scan rate was varied between 20 and 200 mV s^{-1}. The resulting data were analysed using the Randles-Sevick equation, where the peak current was plotted as a function of the square root of the scan rate. In addition, the peak current was plotted as a function of scan rate and the logarithm of the peak current was plotted as a function of the logarithm of the scan rate. From these analyses it is evident that the reduction of *p*-NP is under typical diffusion control for the GCE and GCE/Bi, but on activation of the GCE the rate determining-step becomes a mixed adsorption and diffusion process. Representative voltammograms recorded at different scan rates are presented in Fig. 3(c) for the A-GCE and Fig. 3(d) for the A-GCE/Bi. The corresponding analyses, where the peak current is plotted as a function of scan rate and the associated logarithmic plot are depicted in Fig. S3(a) and (b), respectively for the A-GCE. A linear relationship, with the regression equation, I_p (μA) $= 0.67v$ (mV/s) $+ 9.35$ and R^2 of 0.999 was obtained. Furthermore, the slope of the logarithmic plot was computed as 0.81, indicating the emergence of an adsorption process that can be attributed to the generation of defects and oxygenated sites during the activation process that facilitate adsorption. Interestingly, on electrodeposition of the bismuth dendrites, the mixed diffusion-adsorption process is maintained, as illustrated in Fig. S3(c) and (d). The linear regression equations were determined as, I_p (μA) $= 0.99v$ (mV/s) $+ 11.31$ with R^2 at 0.998 and log $I_p = 0.81$ log $v + 0.43$, R^2 of 0.991, with I expressed as μA and v as mV/s. Here, the slopes at 0.81 for A-GCE and 0.81 for A-GCE/Bi are identical, indicating a similar mixed diffusion adsorption process at the two modified electrodes.

The emergence of an adsorption process was further probed by determining the optimum immersion period and any related memory effects associated with the adsorption of *p*-NP. These experiments are summarised in Fig. S4 for both the A-GCE and the A-GCE/Bi. It is evident in both cases that the current becomes higher on increasing the immersion period before the voltammograms are recorded. The optimum immersion period is approximately 7 min for the A-GCE and the memory effect can be seen in Fig. S4(c). Clear evidence for the accumulation of *p*-NP can be seen in Fig. S4(c) with a significant reduction wave indicating the presence of *p*-NP for the first cycle, and a somewhat lower peak current for the second cycle. The corresponding experiments for the A-GCE/Bi are presented in Fig. S4(b) and (d) and again adsorption is evident. Although the maximum adsorption occurs at a slightly longer time of 8 min, which may indicate a somewhat slower accumulation process at the bismuth dendrite modified surface, prominent peaks are evident for the first cycle with smaller peaks following the second, third and fourth cycles.

On comparing the CVs shown for the A-GCE and A-GCE-Bi, Fig. 3(c) and (d), it is evident that the peak potential increases at a slightly greater rate with increasing scan rate for the A-GCE/Bi. This indicates that the electron-transfer becomes somewhat slower on decorating the activated GCE with the bismuth dendrites. This becomes more evident on plotting the peak potential (E_p) as a function of the natural logarithm of the scan rate (v), as shown in Fig. S4(e). Linear plots were obtained for both the A-GCE and A-GCE/Bi, as illustrated in Fig. S4(f). The linear regression equations were obtained as, E_p (V) $= -0.029$ ln$v$ (mV/s) $- 0.596$ ($R^2 = 0.995$) and E_p (V) $= -0.035$ ln$v$ (mV/s) $- 0.554$ ($R^2 = 0.998$) for the A-GCE and A-GCE/Bi, respectively. The higher slope for the A-GCE/Bi indicates a somewhat slower rate of electron transfer. This is in good agreement with the electrochemical impedance studies which show an
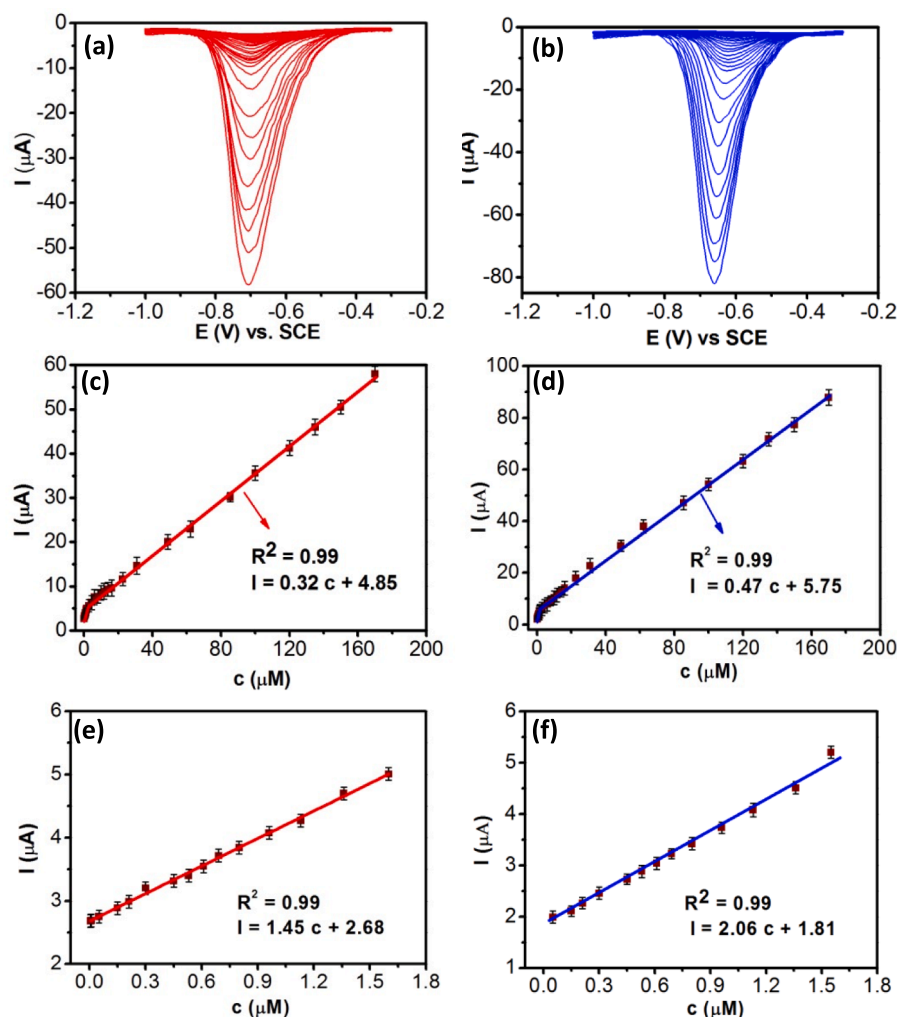
Fig. 4. DPVs recorded as a function of concentration from 0.005 to 170 μM p-NP for **(a)** A-GCE and **(b)** A-GCE/Bi; peak current plotted as a function of concentration for **(c)** A-GCE and **(d)** A-GCE/Bi; peak current plotted as a function of the lower concentrations for **(e)** A-GCE and **(f)** A-GCE/Bi.

increase in the charge transfer resistance on modifying the electrode with the bismuth dendrites.

Using the Laviron method, which is described in Equation (1), where R, T and F represent the gas constant, thermodynamic temperature and Faraday constant, respectively, the αn values were estimated as 0.88 for A-GCE and 0.73 for the A-GCE-Bi. This indicates a significant deviation from the theoretical value of 2.0 arising from a value of 0.5 for α when n is set at 4. However, this may be related to the nature of the p-NP reduction reaction, with an initial slow one-electron transfer step, Eq. (2), followed by the transfer of three electrons, Eq. (3) [28]. Indeed, on assuming n is 1.0, then α values were computed as 0.88 for A-GCE and 0.73 for the A-GCE-Bi, which fall within the likely values for α ($0.1 < \alpha < 0.9$).

$$E_p = E^0 + \left(\frac{RT}{\alpha nF}\right)\ln\left(\frac{RTK_s}{\alpha nF}\right) + \frac{RT}{\alpha nF}\ln\nu \tag{1}$$

$$R-NO_2 + e^- \rightarrow R-NO_2^- \, (\text{fast}) \tag{2}$$

$$R-NO_2^- + 3e^- + 4H^+ \rightarrow R-NHOH + H_2O\,(\text{slow}) \tag{3}$$

It is clear from this analysis that the improved performance of the A-GCE/Bi, Fig. 1, is not related to an increase in the rate of electron transfer. It appears to be more connected with an increase in the surface area of the A-GCE/Bi and the transition to a mixed diffusion-adsorption process, with the bismuth dendrites providing more adsorption sites.

Indeed, on comparing the memory effects in Fig. S4(c) and (d) there is evidence that higher amounts of p-NP are adsorbed at the A-GCE/Bi.

3.4. Performance of sensor

The performance of A-GCE and A-GCE/Bi in the electrochemical detection of p-NP from 0.005 to 170 μM is illustrated in Fig. 4. Here, the data were recorded using differential pulse voltammetry. The voltammograms are depicted in Fig. 4(a) and (b) for the A-GCE and A-GCE/Bi, respectively. In both cases, the peak potentials remain essentially constant and independent of the concentration, while the peak current increases with increasing concentrations of p-NP. On plotting the peak current as a function of the concentration, linear calibration curves were obtained. The linear regression equation for A-GCE/Bi was deduced as, $I_p(\mu A) = 0.47c(\mu M) + 5.75$ ($R^2 = 0.996$) from 1.6 to 170 μM (Fig. 4(d)), while with lower concentrations from 0.005 to 1.6 μM, the linear regression equation became, $I_p(\mu A) = 2.06c(\mu M) + 1.81$ ($R^2 = 0.994$), Fig. 4(f), indicating a much higher gradient (2.06 μA μM^{-1} or 29.4 μA μM^{-1} cm^{-2}, where the geometric surface area was used to compute the current density) at the lower concentrations. Using the well-known expression where LOD = 3σ/sensitivity, the LOD was computed as 0.18 nM.

Similar experiments were carried out for the A-GCE, with the LOD estimated as 0.32 nM. The linear regression at higher concentrations, from 1.6 to 170 μM, was deduced as $I_p(\mu A) = 0.323c(\mu M) + 4.856$, ($R^2 =$

Table 2
Comparison with recently reported sensors for the detection of *p*-NP.

System	Technique	LOD/ nM	Linear Range/μM	Ref
L-Cys/Nd$_2$O$_3$/rGO/GCE	SWV	20	0.05–8 10–50	[30]
Carboxymethylcellulose/ polyaniline/GCE	DPV	53	0.05–100	[31]
polyspirofluorene film/GCE	DPV	10	0.1–120	[32]
rGO-NiCo$_2$O$_4$/aminopropyl-triethoxysilane/GCE	DPV	5	0.005–5	[33]
AgNPs/GCE	DPV	15	0.1–350	[34]
CeMoSe$_2$/GCE	LSV	3.5	0.04–280 300–1980	[26]
Nanoparticle GC film	CV	230	0.5–3.0 3–3000	[35]
Ni$_3$Se$_4$/rGO/ITO	DPV	17.1	0.05–5 5–200	[36]
Pyridine diketopyrrolopyrrole/ GO/GCE	DPV	100	0.5–50 50–163	[37]
CeFeP/GCE	DPV	10	0.1–50	[16]
A-GCE	DPV	0.32	0.005–1.6 1.6–170	
A-GCE/Bi	DPV	0.18	0.005–1.6 1.6–170	This Work

0.999), Fig. 4(c), while at lower concentrations, from 0.005 to 1.6 μM, the linear regression, I_p (μA) = 1.4527c(μM) + 2.68 (R^2 = 0.9976), Fig. 4 (e) was obtained. As illustrated in Table 2, where the linear regions and LOD values are presented for a variety of recently reported sensors for the detection of *p*-NP, this simple activated GCE and the activated GCE with bismuth dendrites compare very well. Moreover the A-GCE/Bi has

an impressive sensitivity of 29.4 μA μM^{-1} cm^{-2}. The typical concentrations of *p*-NP in aquatic environments can vary from 0.43 μg L^{-1} in rivers [3] to concentrations ranging from 0.22 to 1.65 μg L^{-1} in snow covered regions [29]. Therefore, the LOD of 0.18 nM obtained for the A-GCE/Bi, coupled with its good sensitivity of 29.4 μA μM^{-1} cm^{-2} makes it a suitable sensor for these environments.

The selectivity of the A-GCE/Bi sensor is represented in Fig. 5(a), where the peak current recorded for 100 μM *p*-NP is designated as I_o and the current recorded in the presence of the interferent is I, with a value of unity indicating no interference. In these experiments, a 100 μM solution of *p*-NP in the presence of a 10-fold excess of the interferents except for *ortho*-nitrophenol (*o*-NP) and the nitro-based drug metronidazole (MTZ). These two compounds were maintained at 100 μM. Very good selectivity can be seen in the presence of acetates, sulfates, nitrates and carbonates. Likewise good selectivity is seen on the addition of hydrocortisone (HC), ascorbic acid (AA) and glucose (Glu). Nevertheless some interference is evident with *o*-NP and MTZ, as shown in Fig. 5(c) and (d), respectively. This is not surprising as these two nitro-based compounds can be electrochemically reduced and the reduction process involves the conversion of the nitro groups to a hydroxylamine groups. The selectivity was further explored using a spiking and recovery approach, where a known amount of *p*-NP was added and then the sensors were employed to determine the concentration of *p*-NP in the sample. Both deionised water and tap water were employed and the results are summarised in Table 3. Good recovery, varying from 96.5 to 106.7 %, was achieved with the A-GCE/Bi with added concentrations of 3, 6 and 10 μM *p*-NP. The stability of the A-GCE/Bi is illustrated in Fig. 5(b), where the peak current is shown as a function of the cycle number for both a stagnant solution and an agitated solution. For comparative purposes, data for the A-GCE are
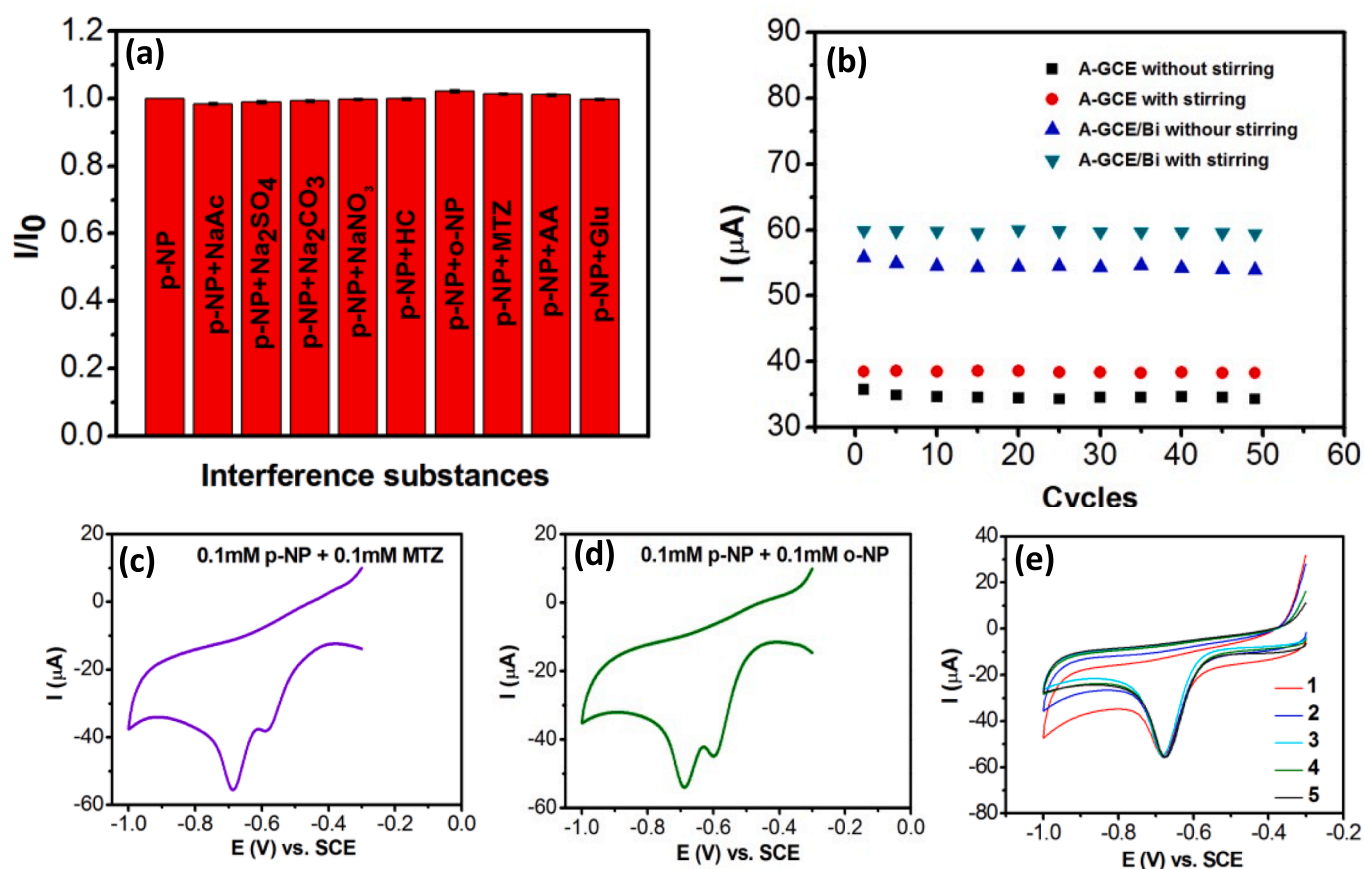

Fig. 5. (a) Selectivity, I/I_o, for A-GCE/Bi in the presence of different interference substances; (b) peak current plotted as a function of cycle number for A-GCE and A-GCE/Bi with and without stirring in 100 μM *p*-NP; (c) CV recorded for A-GCE/Bi in 100 μM *p*-NP and 100 μM MTZ; (d) CV recorded for A-GCE/Bi in 100 μM *p*-NP and 100 μM *o*-NP; (e) CVs recorded for A-GCE/Bi in 100 μM *p*-NP following removal and deposition of new Bi dendrites.

Table 3
Determination of *p*-NP in deionised and tap water using A-GCE and A-GCE/Bi.

Sensor	Sample	Added/ µM	Found/ µM	Recovery
A-GCE	Deionised water	3.0	3.18	106.0 %
		6.0	6.22	103.7 %
		10.0	9.75	97.5 %
A-GCE	Tap water	3.0	2.89	96.3 %
		6.0	6.55	105.3 %
		10.0	9.95	99.5 %
A-GCE-Bi	Deionised water	3.0	3.14	104.7 %
		6.0	5.87	97.8 %
		10.0	10.33	103.3 %
A-GCE-Bi	Tap water	3.0	3.20	106.7 %
		6.0	5.79	96.5 %
		10.0	9.86	98.6 %

also shown. In both cases very good stability is observed with little change in the peak current over 50 cycles.

One of the advantages of decorating the A-GCE with bismuth dendrites is that the bismuth can be easily oxidised and removed from the sensor, and this can be later followed by the deposition of fresh dendrites at the A-GCE. In order to explore the potential of this regeneration step, the bismuth was oxidised at 0.60 V for 10 min and then a fresh layer of bismuth was electrodeposited from the acidified 1.0 mM Bi(NO$_3$)$_3$ solution. The newly regenerated A-GCE/Bi was then used in the detection of 100 µM *p*-NP. These steps were repeated a total of five times and the corresponding data are shown in Fig. 5(e). Here it is evident that the five voltammograms are very similar, giving nearly identical peak currents and peak potentials. This clearly shows that the A-GCE/Bi sensor can be easily and readily regenerated and this may be very relevant in complex environments where the sensor may be poisoned.

4. Conclusions

In this work, we show that a simple A-GCE combined with a 400 s period for the electrodeposition of bismuth can be used to give the effective detection of *p*-NP in aqueous systems. An impressive limit of detection of 0.18 nM and sensitivity of 29.4 µA µM^{-1} cm^{-2} coupled with very good reproducibility, repeatability, recovery in water and acceptable selectivity were achieved with this simple approach. The good detection in the presence of the bismuth dendrites was attributed to enhanced adsorption of the *p*-NP. While various electrocatalytic materials have been synthesised and then drop-cast onto GCE to form a myriad of electrochemical sensors, this simple approach avoids the need for drop-casting. Moreover, the bismuth dendrites can be easily regenerated making this combination suitable in complex media that may otherwise contaminate or poison the electrode surface.

Declaration of Competing Interest

The authors declare that they have no known competing financial interests or personal relationships that could have appeared to influence the work reported in this paper.

Data availability

Data will be made available on request.

Appendix A. Supplementary data

Supplementary data to this article can be found online at https://doi.org/10.1016/j.microc.2023.109453.

References

[1] J. Li, D. Kuang, Y. Feng, F. Zhang, Z. Xu, M. Liu, A graphene oxide-based electrochemical sensor for sensitive determination of 4-nitrophenol, J. Hazard. Mater. 201–202 (2012) 250–259, https://doi.org/10.1016/j.jhazmat.2011.11.076.

[2] H. Yin, Y. Zhou, S. Ai, X. Liu, L. Zhu, L. Lu, Electrochemical oxidative determination of 4-nitrophenol based on a glassy carbon electrode modified with a hydroxyapatite nanopowder, Microchim. Acta 169 (2010) 87–92, https://doi.org/10.1007/s00604-010-0309-1.

[3] R. Peñalver, M.R. Jacobs, S. Hegarty, F. Regan, Assessment of anthropogenic pollution by monitoring occurrence and distribution of chemicals in the river Liffey in Dublin, Environ. Sci. Pollut. Res. 28 (2021) 53754–53766, https://doi.org/10.1007/s11356-021-14508-y.

[4] M. Kulkarni, A. Chaudhari, Microbial remediation of nitro-aromatic compounds: an overview, J. Environ. Manage. 85 (2007) 496–512, https://doi.org/10.1016/j.jenvman.2007.06.009.

[5] R. Dai, J. Chen, J. Lin, S. Xiao, S. Chen, Y. Deng, Reduction of nitro phenols using nitroreductase from E. coli in the presence of NADH, J. Hazard. Mater. 170 (2009) 141–143, https://doi.org/10.1016/j.jhazmat.2009.04.122.

[6] T. Cáceres, K. Venkateswarlu, M. Megharaj, Acute toxicity of the insecticide methyl parathion and its hydrolytic product p-nitrophenol to the native Australian cladoceran Daphnia carinata, Ecotoxicology 28 (2019) 680–685, https://doi.org/10.1007/s10646-019-02064-8.

[7] J.-H. Yen, K.-H. Lin, Y.-S. Wang, Acute lethal toxicity of environmental pollutants to aquatic organisms, Ecotoxicol. Environ. Saf. 52 (2002) 113–116, https://doi.org/10.1006/eesa.2002.2167.

[8] Z. Yan, W. Wang, J. Zhou, X. Yi, J. Zhang, X. Wang, Z. Liu, Screening of high phytotoxicity priority pollutants and their ecological risk assessment in China's surface waters, Chemosphere 128 (2015) 28–35, https://doi.org/10.1016/j.chemosphere.2015.01.015.

[9] A. Peñalver, E. Pocurull, F. Borrull, R.M. Marcé, Solid-phase microextraction coupled to high-performance liquid chromatography to determine phenolic compounds in water samples, J. Chromatogr. A 953 (2002) 79–87, https://doi.org/10.1016/S0021-9673(02)00113-9.

[10] P.-P. Zhang, Z.-G. Shi, Y.-Q. Feng, Determination of phenols in environmental water samples by two-step liquid-phase microextraction coupled with high performance liquid chromatography, Talanta 85 (2011) 2581–2586, https://doi.org/10.1016/j.talanta.2011.08.021.

[11] E. Tesarova, D. Sykora, Z. Voznakova, GC and HPLC determination of nitrophenol related pesticides, Fresenius Environ. Bull. 4 (1995) 609–616.

[12] A. Niazi, A. Yazdanipour, Spectrophotometric simultaneous determination of nitrophenol isomers by orthogonal signal correction and partial least squares, J. Hazard. Mater. 146 (2007) 421–427, https://doi.org/10.1016/j.jhazmat.2007.03.063.

[13] R. Krishnamoorthy, K. Muthumalai, T. Nagaraja, R.T. Rajendrakumar, S.R. Das, Chemically exfoliated titanium carbide MXene for highly sensitive electrochemical sensors for detection of 4-Nitrophenols in drinking water, ACS Omega 7 (2022) 42644–42654, https://doi.org/10.1021/acsomega.2c06505.

[14] D.S. Rana, S. Kalia, R. Kumar, N. Thakur, R.K. Singh, D. Singh, Two-dimensional layered reduced graphene oxide-tungsten disulphide nanocomposite for highly sensitive and selective determination of para nitrophenol, Environ. Nanotechnol. Monit. Manag. 18 (2022), 100724, https://doi.org/10.1016/j.enmm.2022.100724.

[15] N.S. Gudipati, S. Vanjari, S. Korutla, R.R. Tammineni, S. Challapalli, Electrochemical detection of 4-nitrophenol on nanostructured CuBi$_2$O$_4$ with plausible mechanism supported by DFT calculations, J. Environ. Chem. Eng. 10 (2022), https://doi.org/10.1016/j.jece.2022.108758.

[16] S. Gopi, K. Yun, Cerium-iron phosphate nano flower bifunctional electrocatalyst for efficient electrochemical detection and catalytic reduction of hazardous 4-nitrophenol, J. Environ. Chem. Eng. 10 (2022), https://doi.org/10.1016/j.jece.2022.108938.

[17] B. Healy, F. Rizzuto, M. de Rose, T. Yu, C.B. Breslin, Electrochemical determination of acetaminophen at a carbon electrode modified in the presence of β-cyclodextrin: role of the activated glassy carbon and the electropolymerised β-cyclodextrin, J. Solid State Electrochem. 25 (2021) 2599–2609, https://doi.org/10.1007/s10008-021-05044-3.

[18] T. Yu, O. Fenelon, K.M. Herdman, C.B. Breslin, The electrochemical detection of 4-chloro-2-methylphenoxyacetic acid (MCPA) using a simple activated glassy carbon Electrode, J. Electrochem. Soc. 169 (2022), https://doi.org/10.1149/1945-7111/ac5c03.

[19] S. Faraezi, M.S. Khan, F.Z. Monira, A. al Mamun, T. Akter, M. al Mamun, M. M. Rabbani, J. Uddin, A.J.S. Ahammad, Sensitivity Control of hydroquinone and catechol at poly(Brilliant Cresyl Blue)-modified GCE by varying activation conditions of the GCE: an experimental and computational study, Chem. Eng. 6 27 (2022), https://doi.org/10.3390/chemengineering6020027.

[20] Y. Lu, C. Bao, J. Zou, J. Xiao, W. Zhong, Y. Gao, Highly sensitive electrochemical sensor for sunset yellow based on electrochemically activated glassy carbon electrode, Molecules 27 (2022) 5221, https://doi.org/10.3390/molecules27165221.

[21] A. Rana, A. Baig, T.A. Saleh, Electrochemically pretreated carbon electrodes and their electroanalytical applications – a review, J. Electroanal. Chem. 833 (2019) 313–332, https://doi.org/10.1016/j.jelechem.2018.12.019.

[22] T. Yu, L. Glennon, O. Fenelon, C.B. Breslin, Electrodeposition of bismuth at a graphene modified carbon electrode and its application as an easily regenerated sensor for the electrochemical determination of the antimicrobial drug metronidazole, Talanta 251 (2023), 123758, https://doi.org/10.1016/j.talanta.2022.123758.

[23] A. Królicka, R. Pauliukaiteppproaches the limit, I. Svancara, R. Metelka, A. Bobrowski, E. Norkus, K. Kalcher, K. Vytřas, Bismuth-film-plated carbon paste electrodes, Electrochem. Commun. 4 (2002) 193–196, https://doi.org/10.1016/S1388-2481(01)00301-0.

[24] I. Švancara, L. Baldrianová, E. Tesařová, S.B. Hočevar, S.A.A. Elsuccary, A. Economou, S. Sotiropoulos, B. Ogorevc, K. Vytřas, Recent advances in anodic stripping voltammetry with bismuth-modified carbon paste electrodes, Electroanalysis 18 (2006) 177–185, https://doi.org/10.1002/elan.200503391.

[25] Z. Zou, A. Jang, E. MacKnight, P.-M. Wu, J. Do, P.L. Bishop, C.H. Ahn, Environmentally friendly disposable sensors with microfabricated on-chip planar bismuth electrode for in situ heavy metal ions measurement, Sens Actuators B Chem. 134 (2008) 18–24, https://doi.org/10.1016/j.snb.2008.04.005.

[26] S. Ramki, R. Sukanya, S.-M. Chen, M. Sakthivel, J.Y. Wang, Simple hydrothermal synthesis of defective CeMoSe₂ dendrites as an effective electrocatalyst for the electrochemical sensing of 4-nitrophenol in water samples, New J. Chem. 43 (2019) 17200–17210, https://doi.org/10.1039/c9nj03891d.

[27] R. Sundaresan, V. Mariyappan, S.-M. Chen, B. Ramachandran, R. Paulsamy, R. Rasu, Construction of an electrochemical sensor towards environmental hazardous 4-nitrophenol based on Nd(OH)₃-embedded VSe₂ nanocomposite, Environ. Sci. Pollut. Res. (2023), https://doi.org/10.1007/s11356-023-25688-0.

[28] N. Čėnas, A. Nemeikaitė-Čėnienė, L. Kosychova, Single- and two-electron reduction of nitroaromatic compounds by flavoenzymes: Mechanisms and implications for cytotoxicity, Int. J. Mol. Sci. 22 (2021), https://doi.org/10.3390/ijms22168534.

[29] S. Levshina, Petroleum products and phenols in snow cover in Khabarovsk, Southern Russian far east, Water Air Soil Pollut. 223 (2012) 3553–3563, https://doi.org/10.1007/s11270-012-1136-2.

[30] Z. Sabir, M. Akhtar, S. Zulfiqar, S. Zafar, P.O. Agboola, S. Haider, S.A. Ragab, M.F. Warsi, I. Shakir, L-Cysteine functionalized Nd₂O₃/rGO modified glassy carbon electrode: a new sensing strategy for the rapid, sensitive and simultaneous detection of toxic nitrophenol isomers, Synth. Met. 277 (2021), 116774, https://doi.org/10.1016/j.synthmet.2021.116774.

[31] K.A. Alamry, A. Khan, M.A. Hussein, S.Y. Alfaifi, Sensitive electrochemical detection of toxic nitro-phenol in real environmental samples using enzymeless oxidized-carboxymethyl cellulose-sulfate/sulfated polyaniline composite based electrode, Microchem. J. 172 (2022), 106902, https://doi.org/10.1016/j.microc.2021.106902.

[32] Y. Fang, D. Wang, X. Lv, X. Xu, H. Zhou, P. Liu, B. Cui, L. Wang, Simultaneous electrochemical determination of nitrophenol isomers Based on spirofluorene - based microporous polymer film modified electrodes through one-step electropolymerization strategy, Sens Actuators B Chem. 333 (2021), 129568, https://doi.org/10.1016/j.snb.2021.129568.

[33] M.Z.H. Khan, J. Zhu, X. Liu, Reduced graphene oxide-conjugated urchin-like NiCo₂O₄ nanostructures for individual detection of o-nitro and p-amino phenol, ACS Omega 4 (2019) 11433–11439, https://doi.org/10.1021/acsomega.9b00804.

[34] C. Karuppiah, S. Palanisamy, S.-M. Chen, R. Emmanuel, M.A. Ali, P. Muthukrishnan, P. Prakash, F.M.A. Al-Hemaid, Green biosynthesis of silver nanoparticles and nanomolar detection of p-nitrophenol, J. Solid State Electrochem. 18 (2014) 1847–1854, https://doi.org/10.1007/s10008-014-2425-z.

[35] P. Wang, J. Xiao, A. Liao, P. Li, M. Guo, Y. Xia, Z. Li, X. Jiang, W. Huang, Electrochemical determination of 4-nitrophenol using uniform nanoparticle film electrode of glass carbon fabricated facilely by square wave potential pulses, Electrochim. Acta 176 (2015) 448–455, https://doi.org/10.1016/j.electacta.2015.07.054.

[36] S. Wang, T. Zhang, L. Jia, P. Yang, P. He, F. Xiao, P. Zhou, Y. Wang, X. Wang, Electrochemical reduction of nickel selenide/reduced graphene oxide nanocomposites: Highly sensitive detection of 4-nitrophenol, Microchem. J. 186 (2023), 108252, https://doi.org/10.1016/j.microc.2022.108252.

[37] L. Jia, J. Hao, S. Wang, L. Yang, K. Liu, Sensitive detection of 4-nitrophenol based on pyridine diketopyrrolopyrrole-functionalized graphene oxide direct electrochemical sensor, RSC Adv. 13 (2023) 2392–2401, https://doi.org/10.1039/d2ra07239d.